Growth of vapor-deposited cobalt films on Pt(111) studied by scanning tunneling microscopy

P. Grütter and U. T. Dürig
IBM Research Division, Zurich Research Laboratory, 8803 Rüschlikon, Switzerland
(Received 19 July 1993)

The initial nucleation and subsequent growth of vapor-deposited Co on Pt(111) has been studied by scanning tunneling microscopy and Auger-electron spectroscopy. When deposited at room temperature, Co nucleates spatially in a homogeneous manner and then grows quasi-layer-by-layer up to a coverage of $\Theta=3$ monolayers. For $\Theta>3$ monolayers, a three-dimensional island growth mode is observed. From a detailed analysis of the observed island shapes we present direct evidence that Co grows in a hcp pattern on Pt(111) after the third layer. The nucleation of Co at a deposition temperature above 300 K is strongly influenced by the appearance of a Co-induced surface reconstruction of Pt(111). This reconstruction leads to a dendritic growth of Co deposited at 400 K. Fingers of Co 3–5 nm wide and up to 250 nm long can be observed. The influence of the Pt reconstruction on the growth becomes smaller at higher deposition temperatures, leading to compact, triangular Co islands at 600 K.

I. INTRODUCTION

Co/Pt multilayers are candidates for high-density magneto-optical (MO) recording media due to their perpendicular magnetic anisotropy and large Kerr rotation at small optical wavelengths.[1] The perpendicular magnetic anisotropy necessary for MO recording is observed when the Co layers are thinner than about 1.2 nm, with the largest values of the anisotropy reported for vapor-deposited, (111) fcc textured superlattices. Magnetic properties optimized for MO recording are obtained from a multilayer structure consisting of about 20 repetitions of Co layers only 0.4 nm thick (or about two atomic layers) separated by a Pt layer typically 1.3 nm thick.[2]

The origin of the perpendicular anisotropy observed in many transition-metal/noble-metal multilayers such as Co/Pt, Co/Au or Co/Pd is controversial and not well understood. Interface or surface anisotropy as a result of the broken symmetry at interfaces,[3,4] magnetoelastic anisotropy due to strain,[5,6] or magnetocrystalline anisotropy as a result of alloyed or compositionally mixed interfaces[7,8] have been proposed. These suggestions were based on theoretical arguments supported by structural studies and magnetic measurements. Most structural studies on these multilayers have been performed either by high-resolution cross-sectional transmission electron microscopy or by diffraction-based techniques such as x-ray diffraction, low-energy electron diffraction (LEED) or reflection high-energy electron diffraction (RHEED). In order to interpret the results of these techniques, a model of the structure, which is difficult to confirm directly by any of these techniques, has to be assumed. Furthermore, the magnetic properties are found to be structure sensitive and dependent on the Co-layer thickness.[9] The uncertainty regarding the structure of these films is one of the main reasons for the unsatisfactory and sometimes contradictory explanations of experimental results.

Scanning tunneling microscopy (STM) is known to be well suited to study the heteroepitaxy of metal systems because of its high lateral resolution and inherent real-space imaging capabilities.[10,11] Thus STM studies of Ni, Co, and Fe on Au(111) have revealed a remarkable influence of the Au(111) $22\times\sqrt{3}$ reconstruction on the resulting film structure.[12] A different STM study showed that Co on Cu(111) grows in the form of bilayer islands that do not coalesce, but actually form a granular film, even though the growing film remains epitaxial and crystalline to the extent tested by diffraction techniques.[13] Surprisingly, no real-space study of the structure has been reported for the technologically most promising system: Co grown on a Pt substrate with (111) texture.

In this paper we investigate the growth of the first few layers of Co on a Pt(111) single crystal by ultrahigh vacuum STM and Auger-electron spectroscopy (AES). We characterize the growth modes, the influence of annealing, and the effect of substrate temperature during deposition. Characterizing and understanding the microstructure of the first few layers of Co deposited on Pt provides significant insight into the evolution of multilayer structures. It also forms the basis for understanding the evolution of magnetic microstructures determined by spin-polarized scanning electron microscopy as a function of Co film thickness and morphology.[14]

II. INSTRUMENTATION AND SAMPLE PREPARATION

All STM measurements presented in this paper were performed at room temperature at a pressure of less than 8×10^{-11} mbar.[15] The STM chamber is connected to a sample preparation chamber equipped with a cylindrical mirror AES, an ion gun, a sample annealing station,[16] and a water-cooled electron-beam Co evaporator. The pressure during evaporation was below 3×10^{-10} mbar. The evaporator flux was calibrated by three independent methods: AES, optical transmission, and atomic force microscopy, each agreeing with the others to within 10%. Coverage determined by STM is in accordance with the values expected from this calibration. In the experiments presented here we used an evaporation rate of

0.1 ± 0.01 monolayer (ML) per minute, where 1 ML is defined as 0.205 nm. In bulk Co this would correspond to one {111} layer. For each Co coverage investigated we started with a freshly prepared Pt substrate.

The substrate we used is a polished Pt(111) single crystal cut to the dimensions of $5\times0.1\times0.05$ mm^3. These unusual dimensions are necessary because this sample also serves as a cantilever, allowing us to perform *in situ* interaction force measurements.[17] Initial removal of C impurities was done efficiently by dosing the Pt at 800 K with 1×10^{-5} mbar of O_2 for 30 s. Several cycles of 10-min, 1-keV, 10-μA/mm^2 Ne sputtering followed by 10-min anneals to 1250 K were performed to clean the Pt(111) surface. AES spectra then showed no traces of contaminants. We have found that in order to obtain large, flat terraces separated by straight steps it is important to cool the sample slowly. We used a cooling rate of about 100 K per minute. If we simply turn off the heating power to terminate annealing, the Pt cantilever, with its small thermal mass, cools too quickly at approximately 200 K per second. This rapid cooling gives rise to thermal stress in the sample which results in a buckled surface topography.

Mechanically sharpened Ir and etched W tips were used as tunneling tips. No difference between these tips was detected in the constant current topographs. Tip shaping was performed *in situ*. For this purpose -150 V was applied to a clean sample and the STM was operated in a field-emission mode at current levels up to 50 nA. After this treatment tunneling barrier heights of 3.5–4 eV were observed. We always measured the barrier height using the modulation technique simultaneously with the constant current images to check the quality of the tunneling junction. Unless otherwise indicated, all images were acquired at a constant tunneling current of 0.3 nA and a sample voltage of -100 mV. Typical scan rates are 1–2 lines per second.

III. EXPERIMENTAL RESULTS

Figure 1 is a STM image of the clean Pt(111) surface. After annealing we observe large flat terraces separated by sequences of closely separated steps. When large scan-area images are analyzed, the average surface tilt angle determined from STM images correlates well with the crystal miscut of 0.5° determined from x-ray diffraction. The apparent phase separation of flat and stepped surfaces[18]—also called step bunching—is attributed to an attractive interaction between steps and has previously been observed for Au(111).[19]

Occasionally we were able to image the close-packed atomic structure of the Pt(111) surface [Figs. 1(b) and 1(c)]. This allows us to determine the precise orientation of the substrate. We find that most steps observed run parallel to the ⟨110⟩ direction. Figure 1(b) was obtained at a tunneling junction resistance of 1 MΩ (sample voltage -10 mV) and represents raw data. One readily observes stripes which are typical for telegraph-type height fluctuations. The stripe structure correlates with associated barrier height changes from 3.5 to 4.7 eV. We attribute this to subtle subnanometer changes in the atomic tip configuration. Close examination, however, indicates that atomic resolution is never lost. As often observed in STM topographs, steps are smeared out over a distance of about 1–2 nm due to the extended size of the atomic cluster forming the end of tip. The image in Fig. 1(c) is slightly low-pass filtered to suppress noise with spatial frequencies smaller than one-tenth of a lattice constant. It clearly shows the expected hexagonal arrangement of Pt(111) surface atoms. In the following we will describe the growth mode and annealing properties of Co.

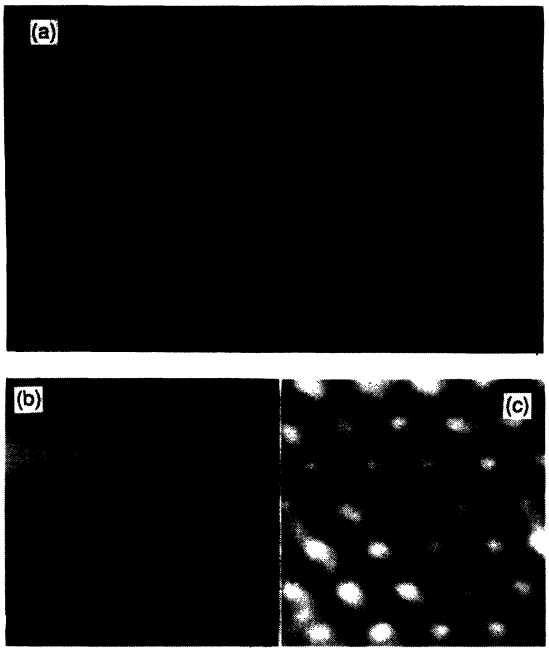

FIG. 1. (a) 1200×1200-nm^2 image of well-annealed Pt(111). Black (white) lines correspond to a single atomic steps down (up) when viewed from left to right. (b) 15×15-nm^2 image showing atomic resolution across a Pt(111) step. Horizontal stripes are due to subtle changes of the tip. (c) Low-pass filtered section of (b), showing Pt(111) atoms.

A. Co films grown at 300 K

When Co is deposited at room temperature on the Pt(111) surface, spatially uniformly distributed nucleation is observed. At present, we cannot determine whether the nucleation is homogeneous or, alternatively, induced by randomly distributed defects (such as residual C contaminants below the AES detection limit). At a coverage of $\Theta=0.2$ ML, [Fig. 2(a)] Co islands are Poisson distributed in size with a mean area of about 53 nm^2 and an average separation of 20 nm. Thus the average distance a Co atom travels at room temperature on a Pt(111) surface before it attaches to a Co island is at least 20 nm. In the following we will refer to this distance as the "diffusion length." We can easily distinguish between Co and Pt based on the difference in step heights (0.205 vs 0.226 nm, respectively). This can clearly be seen in Fig. 2(b)—acquired after the deposition of 0.57 ML of Co—where some of the Co islands are adjacent to the lower side of

the Pt steps. The larger Co islands have very small second-layer Co islands (termed "clusters" in the following) on top of them. These two-dimensional clusters have properties, to be described in the following, which set them apart from regular Co islands. The total area covered by these second-layer Co clusters at $\Theta = 0.57$ ML corresponds to 0.06 ML. The size of these clusters is Poisson distributed with a mean area of 9 nm^2. Surprisingly, first-layer Co exhibits these small clusters at a nearly constant number density with no change in cluster height (0.2 nm), mean area (9 nm^2), and average separation (5 nm) up to completion of the second Co layer [Figs. 2(c) and 2(d)]. These clusters do not correspond to a thermal equilibrium configuration. Instead, they appear because of hampered interlayer mass transport, as will be shown later by performing annealing studies. These studies indicate that the clusters decorate depressions, the origin of which most probably can be attributed to misfit dislocations in the first Co layer. Preferential decoration of sites distorted from perfect (111) surface crystallography has previously been observed for Ni, Fe, and Co deposited on Au(111) by STM.[12]

The observation of these clusters indicates that the first-layer defects (i.e., depressions) have a rather high capture probability and a high escape barrier for Co adatoms diffusing on first-layer Co islands at room temperature. The experimental observation that the number density and size of clusters are independent of coverage can be understood if one makes the reasonable assumption that the capture probability for Co adatoms arriving from the vapor phase and diffusing on a perfect (111) Co surface is smaller than the corresponding number for the defects. As soon as all the localized depressions are decorated, atoms arriving on the first-layer Co islands diffuse until they fall over an island edge, contributing to first-layer growth. Clusters, as a result of their small area, have a very small capture probability and thus do not grow substantially in size. This size argument, of course, could also be applied to the depressions, which are small. One would then not understand why they have a large capture rate, as inferred from the observation of cluster decoration. Depressions, however, are expected to have a large capture rate as a consequence of a larger sticking probability for diffusing Co adatoms. This is in analogy to the driving forces leading to preferential incorporation of adatoms at steps—depressions can be viewed as degenerate holes in the Co island. Furthermore, an effective area substantially larger than the 9 nm^2 inferred from experiment is expected. This is due to long-ranged elastic strain fields associated with a defect which affects the diffusion direction of adatoms landing from the vapor phase. Together, these two factors are expected to lead to a capture rate for the depressions which is substantially larger than that of the perfect (111) surface.

First-layer islands grow continuously with increasing

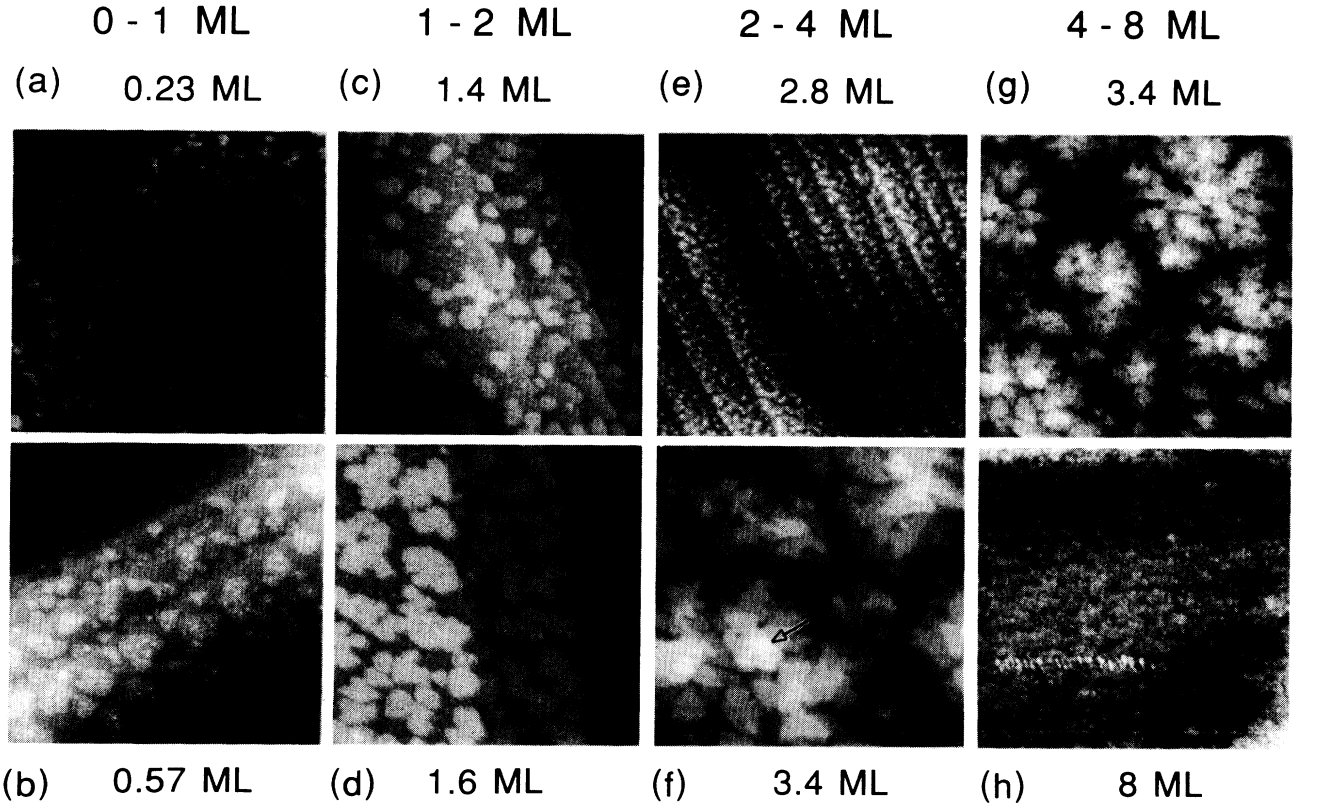

FIG. 2. Vapor deposition of Co on Pt(111) at 300 K. All images are 200×200 nm^2, except (g) and (h), which are 400×400 nm^2 in size. The arrow in (f) points to triangles stacked *UDUD* · · · (see text).

coverage until a complete layer is formed. After percolation at $\Theta = 0.8$ ML, nucleation (probably at clusters) of randomly distributed second-layer islands sets in. These islands grow with increasing coverage, in contrast to the clusters, since capture probability increases with size [Figs. 2(c) and 2(d)]. This sequence repeats itself accordingly; third-layer islands start to grow after percolation of second-layer islands at $\Theta = 1.8$ ML. Note, however, that no third-layer clusters are observed on the second Co layer.

This correlation of the nucleation of next-layer islands with the percolation of the previous-layer islands is attributed to a slightly repulsive barrier to atoms becoming incorporated into the lower side of a step when approaching it from the upper side.[20] The width of percolated islands (of the order of 20 nm) at the nucleation threshold is thus not the diffusion length of Co on Co. If a step is reflective, an atom may reside on the island for a considerable time and in effect diffuse a distance many times larger than the island dimension before falling over the edge. The island topology effectively determines the distance traveled: next-layer island nucleation and simultaneous percolation of the previous layer is thus no coincidence.[20]

In the following we will use the term "quasi-layer-by-layer" to describe this growth mode since substantial next-layer growth starts only after near completion of the previous one. Compared to first-layer islands, second-layer islands show a strong preference for edges along the $\langle 110 \rangle$ directions. Furthermore, substantially fewer third-layer clusters are observable. These general characteristics are even more pronounced for the third layer, where most steps are oriented along the $\langle 110 \rangle$ directions and hardly any fourth-layer clusters are present.

Pt steps do not seem to have a major effect on the growth characteristics, as can be seen by comparing Figs. 2(e) and 3. The images of Fig. 3 were acquired on the same film as was Fig. 2(e), but on a different part of the sample with a lower step density. The growth of this 2.8-ML-thick Co film is not influenced by the presence of steps or screw dislocations on the Pt surface, and is identical on large, flat terraces or stepped surfaces.

We occasionally observe a hexagonal pattern on the second-layer islands with a hexagon side length of 4.1 nm [Fig. 4(a)]. This pattern is observed exclusively on second-layer islands. An interpretation in terms of a Moiré effect as a result of a reduced second-layer lattice spacing suggests itself, analogous to similar observations of a single graphite layer on Pt(111).[21] Inserting the observed periodicity into the Moiré formula[22] yields a reduction of the second-layer lattice spacing by 6% rela-

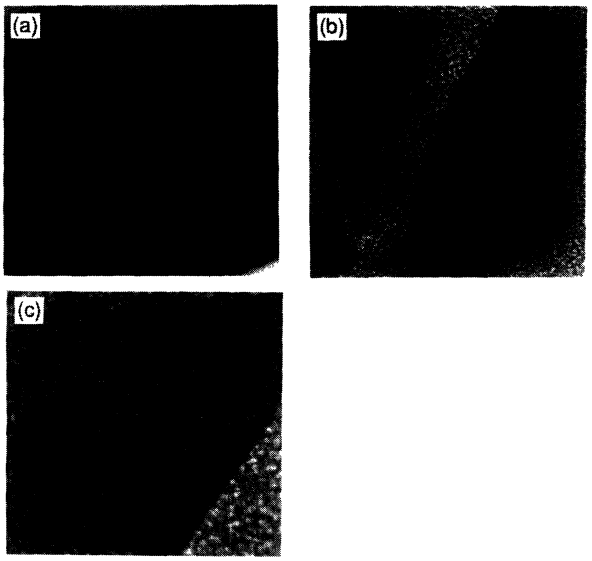

FIG. 3. Images of 2.8-ML Co on Pt(111) at a substrate region with a high density of screw dislocations. (a) 1000×1000 nm^2, (b) 400×400 nm^2, and (c) 200×200 nm^2.

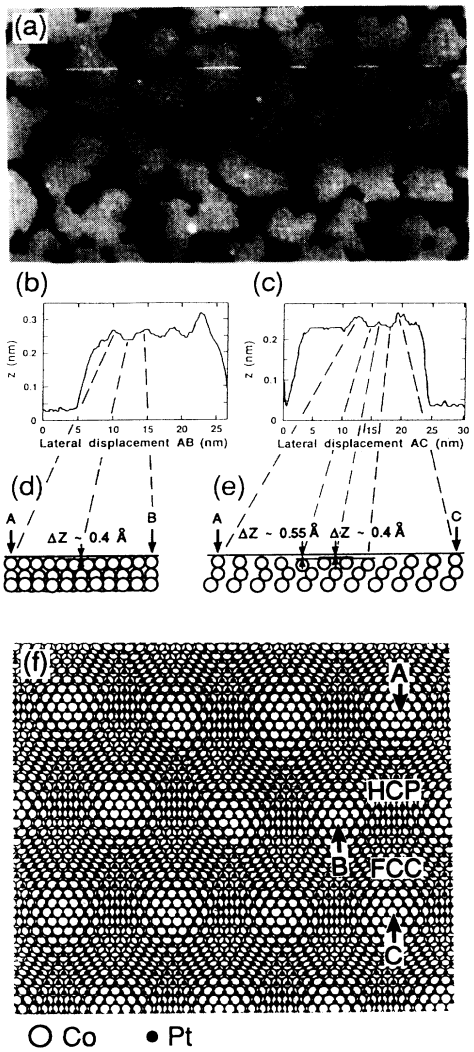

FIG. 4. 200×120-nm^2 image of 1.6 ML of Co on Pt(111) showing Moiré fringes. (a) top view; (b) experimental trace (raw data) along same direction as AB in 4(f); (c) experimental trace (raw data) along same direction as AC in (f); (d) cross section along AB in (f); (e) cross section along AC in (f); and (f) top view of the hard-sphere model of the atomic arrangement of the Pt(111) substrate, the first, and a second 10% contracted Co layer.

tive to that of the first layer. AES and local tunneling barrier height measurements exclude the presence of contaminants, which might induce a reconstruction of the second layer of Co.

In the following we will model and describe the Moiré pattern. In conjunction with other observations, this will allow us to draw conclusions on the coherency, lattice mismatch, and strain relief mechanisms of the first few Co layers.

Figure 4(f) is a top-view representation of a hard-sphere model of the atomic arrangement of the Pt(111) substrate, the first Co layer, and a contracted second Co layer. (For the sake of better visualization in Figs. 4(d)–4(f), we have chosen a 10% instead of the experimentally determined 6% reduction of the second-layer lattice spacing. This has no consequences for the following discussion.) We note that in this model the z position of second-layer Co atoms is modulated, giving rise to the observed Moiré pattern. Regions with hcp–and fcc-type stacking are separated by lines. We will call these lines "dislocation lines." At the dislocation lines, second-layer Co atoms are aligned on top of first-layer atomic rows [see Figs. 4(d) and 4(e)]. Intersections of the dislocation lines correspond to singular points where second-layer Co atoms assume top positions. Correspondingly, the intersections coincide with local maxima of the topographic height and are observed as a hexagonal lattice of bumps in Fig. 4(a).

This model qualitatively reproduces all experimental observations. This is best seen by comparing cross sections of the model [Figs. 4(d) and 4(e)] with experimental traces [Figs. 4(b) and 4(c)]. The characteristics of the modulation depend on the direction of the cross section [*AB* or *AC* in Fig. 4(f)]. We note that along *AB* (a dislocation line), a sinusoidal height variation is expected [Fig. 4(d)] and indeed observed [Fig. 4(b)]. Along *AC*, a double-peaked sinusoidal structure with a big peak, and a second one that is three to four times smaller, are predicted [Fig. 4(e)]. The big peaks are clearly visible, whereas the smaller ones are close to the noise limit in the experimental trace [Fig. 4(c)].

A perfect Moiré pattern can only be observed for two layers that have a different lattice constant and are coherent, i.e., have no defects. On many of the islands these requirements are met quite well within regions having diameters of up to 20 nm, leading to the observed Moiré fringes in Fig. 4(a). The lattice mismatch and coherency requirement is, however, clearly not fulfilled globally, as can be seen in Fig. 4(a), where on some of the islands the fringes are not observable. Defects may pin the Co lattice into a pseudomorphic lattice spacing rather than the relaxed lattice spacing that gives rise to the Moiré pattern. Alternatively, defects that pin the Co structure locally, but do not prevent the Co layer from adopting its relaxed lattice spacing, will distort the hexagonal Moiré pattern and thus make it difficult to detect. The rather noisy experimental traces [Figs. 4(b) and 4(c)] are an indication that coherency is not perfect, most likely due to first-layer point defects. We know that the first Co layer has a substantially higher defect density than does the second one. (This is concluded from the predominant observation of second-layer clusters. As will be shown in Sec. III B, defects in a layer are decorated by next-layer clusters.)

A related observation pointing to substantial strain in the first layer of Co is the fact that at coverages below 3 ML, Co is always rougher on a 1–5-nm lateral scale than is the Pt substrate. We suspect that this lattice-mismatch-induced buckling might also be the reason for our inability to image directly the Co lattice by STM, and for the rather diffuse LEED patterns observed for $\Theta < 3$ ML. The buckling or roughness and defect structure of ultrathin Co layers has substantial consequences in the interpretation of data acquired by any diffraction technique such as x-ray scattering, LEED, or RHEED. Remember that the average separation of 5 nm between the clusters and hence defects is comparable to the typical coherence length of these scattering techniques. This will strongly influence line shapes and intensities.

Let us summarize the lattice strain relief mechanisms observed in the first three Co layers as deduced from the observation of defects decorated by clusters and the detailed analysis of the Moiré pattern presented above. The first Co layer has a substantial number of defects (i.e., depressions) decorated by clusters. These defects relieve part of the strain arising from the 9.7% lattice mismatch of Co and Pt. The origin of these defects can most probably be traced to misfit dislocations. Nevertheless, the first-layer Co lattice can be locally well defined and coherent over regions with diameters as large as 20 nm, definitely so when covered by a further Co layer. It appears that the growth of the second layer induces rearrangements of the first, thus wiping out many of the first-layer defects. The second Co layer has only few defects, indicating that there is little residual strain. Interpretation of the Moiré pattern observed on second-layer islands implies that two-thirds of the total bulk lattice misfit is accommodated by an isotropic lattice contraction of the second Co layer. The third Co layer is thus quite perfect, the result of which is a very low density of fourth-layer clusters. We cannot exclude a small (less than 4%) lattice contraction of the first or third Co layers, since the resulting Moiré periodicity would be masked by the limited width of islands and the presence of defects. We also wish to emphasize that conclusions regarding the structure of buried layers have to be made with care, since rearrangments not detectable by STM might occur upon a layer being covered by the next layer.

After percolation of third-layer islands, a totally new growth mode sets in. Instead of the previous quasi-layer-by-layer growth, the overview shown in Fig. 2(g) shows that a three-dimensional (3D) island growth mode starts. Pyramids of stacked, roughly triangular islands appear, as indicated in Fig. 2(f). Some of them are more than four atomic levels high, meaning that seven atomic levels are exposed simultaneously. The orientation of these triangles [pointing up (U) or down (D) in Fig. 2(f)] changes from layer to layer—the triangle stacking is $UDUDU\cdots$. From this, one can directly conclude that Co grows in an hcp structure after 3 ML. This is based on the following straightforward argument.

First, the origin of the triangular shape is traced to the

fact that there are two types of steps along the ⟨110⟩ direction on a (111) surface: one type of step belongs to a {111} facet, the second one to a {100} facet. If one of these facets is energetically favored, or, alternatively, has a different growth speed, islands tend to grow in threefold instead of sixfold symmetry. If one now makes the plausible assumption that the same facet orientation is favored independently of the thickness of the Co film a *UDUDU* ··· stacking of triangles can only be the result of a hcp stacking of the Co layers. A fcc stacking would lead to triangles all oriented the same way, i.e., an *UUUU* ··· stacking of triangles.

3D island growth leads to a rather rough appearance. As many as 4–7 Co levels are exposed simultaneously. For an 8-ML Co film [shown in Fig. 2(h)] one can still recognize the step structure of the substrate on large-scale images; it is, however, very different to locate precisely. As a consequence it is difficult to determine the exact number of Co levels exposed, though it seems that thicker films ($\Theta > 6$ ML) tend to become slightly flatter again (the number of simultaneously exposed layers decreases to ≈ 4). Comparing it to the 3.4-ML film imaged at the same magnification [Fig. 2(g)], we note that the thick film [Fig. 2(h)] is more granular. The reason for this is not yet understood.

The shape of Co islands grown at room temperature is the result of striving for thermodynamic equilibrium within kinetic constraints. In the following we will investigate the kinetic limitations by studying the temperature dependence of the structure, either by annealing (see Sec. III B) or growing at elevated substrate temperature (Sec. III C). As will become obvious, kinetics play a major role, since these two experimental paths reveal strikingly different results.

B. Annealing of Co films

Figure 5(a) show 0.57 ML of Co deposited at 300 K. Figure 5(b) shows a representative topography of the same film after a 5-min anneal at 400 K and subsequent slow cooldown. The islands are now more compact in shape, viz. the number of isolated islands is smaller [Fig. 5(b)]. Most of these islands have rather meandering borders with straight-edge segments parallel to the ⟨110⟩ directions of the substrate. Predominant in Fig. 5 is that the Co clusters on top of the Co islands have disappeared.

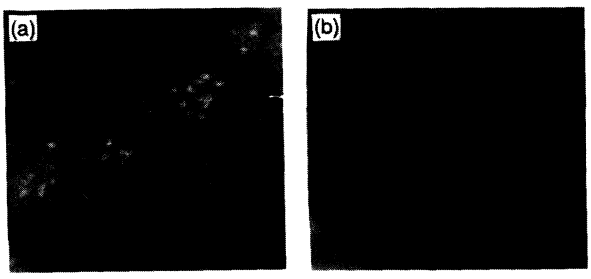

FIG. 5. Annealing study: 100×100-nm^2 image of 0.57 ML of Co on Pt(111): (a) as deposited at 300 K, and (b) after 5 min at 400 K (not at same sample position).

Instead, we now observe small depressions 0.05–0.1 nm deep inside the islands [Fig. 5(b)]. A statistical analysis of STM images shows an 11% surplus island area after annealing. This surplus, however, corresponds to within a statistical error of 1% to the area covered by the clusters.

The separation, density, and size distribution of the depressions is similar to that of the clusters. It thus seems reasonable to argue that for room-temperature deposition the clusters are trapped by the depressions. Comparison of the nucleation properties of Ni, Fe, and CO on Au(111) studied by STM indicate a preference for metals with large lattice misfits to nucleate at sites distorted from the perfect (111) surface crystallography.[12] Annealing allows the clusters to overcome the kinetic limitations imposed by deposition at 300 K, to escape from these shallow traps and to migrate to the energetically preferred Co island edge.

Drastic changes are observed when annealing is performed at temperatures above 750 K. We demonstrate this for a film with $\Theta = 2$ ML. The low-energy (57 eV), surface-sensitive Co AES line disappears completely after only 10 min of annealing at 750 K, while the high-energy (775-eV) Co line intensity decreases monotonically as a function of annealing time. Both the high- (237 eV) and low-energy (64 eV) Pt line intensities increase quickly to a maximum after about 10 min and then remain constant [Fig. 6(a)]. The quick rise of both Pt AES intensities with different inelastic electron mean free paths (0.35 and 0.62 nm) to a near-bulk value indicates that within the probing depth of the high-energy line the sample is pure Pt

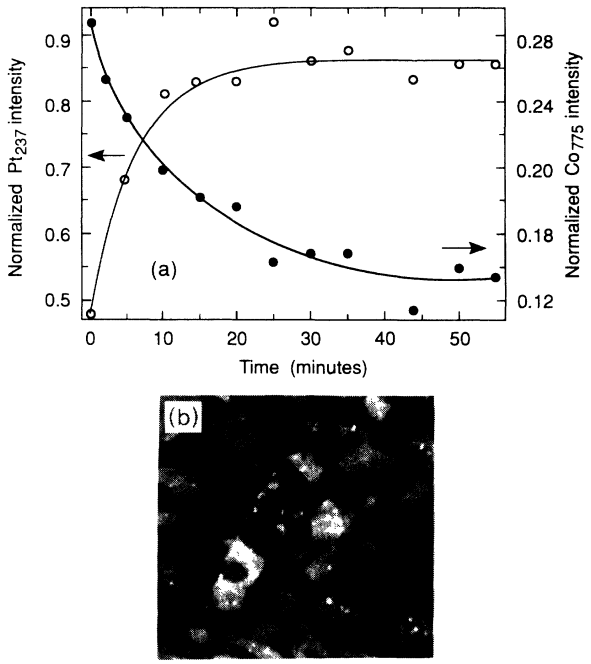

FIG. 6. (a) Evolution of 775-eV Co and 237-eV Pt Auger line intensities as a function of time at an annealing temperature of 750 K. The values are normalized to the measured pure bulk intensities. The interpolating line is a guide to the eye. (b) 400×400-nm^2 image of a 2-ML Co film after 30 min at 750 K.

after 10 min of annealing. The total disappearance of the low-energy Co line (i.e., near-surface Co) cannot be interpreted as a total loss by evaporation of Co into the vacuum because of the persistent observation of the high-energy Co line (with a large probing depth of 1.12 nm). Thus the disappearing Co interdiffuses into the bulk as a function of annealing time. The resulting dilution of Co leads to a monotonic decrease of the high-energy Co AES intensity. Related observations by AES, LEED, and RHEED have previously been reported for Co on Pt(100).[23]

Figure 6(b) shows a STM image after 30 min at 750 K that corroborates the interpretation of interdiffusion. No Co islands are observable, as concluded from the step heights measured. A maze of slightly elevated lines (0.1 nm high), interpreted as stress or dislocation lines, is clearly discernible. From these measurements we cannot determine whether Co diffuses into Pt, or Pt segregates onto the top of the Co islands. In passing, we would like to mention that spin-polarized scanning electron microscopy measurements indicate that Co films annealed at these high temperatures are not ferromagnetic at 300 K.[14]

C. Growth of Co at elevated sample temperatures

From the annealing studies presented above we have concluded that the growth of Co on Pt(111) at room temperature is at least partially kinetically hindered. It is thus obvious that one should try to grow films at elevated temperatures to overcome this limitation. In the following we present results of Co grown on Pt(111) at elevated substrate temperatures T_s. We wish to stress that due to difficulties in calibrating the absolute temperature of the cantilever substrate, the indicated temperatures are subject to an error of ± 50 K. We have to determine the temperature of the cantilever below 800 K by controlling the supplied heating power, since the thermal mass of the cantilever is small compared to that of a thermoelement. The heating power vs temperature curve (determined optically for T_s between 800 and 1500 K) has the reproducibly same linear slope but with statistical variations of the offset. These variations lead to large uncertainties in the absolute temperature. Relative temperature differences, in contrast, can be determined accurately within 10 K, since they depend only on the constant slope of the calibration curve.

When 0.05 ML of Co are evaporated at about 400 K onto Pt(111), a very intricate, surprising morphology is observed [Fig. 7(a)]: large, threefold symmetric Co dendrites grow. These Co dendrites can be up to 250 nm long and 3–5 nm wide. The origin of this growth mode is traced to a Co-induced reconstruction of the Pt(111) surface.[24] Figure 7(b) shows that a reconstruction of the Pt surface accompanies the formation of these Co dendrites.

From the spacing of the two lines [marked by arrows in Fig. 7(b)] and their height we conject that the Pt surface *locally* undergoes a reconstruction similar to the known $22\times\sqrt{3}$ Au(111) reconstruction. In the $22\times\sqrt{3}$ reconstruction, the registry of Au surface atoms varies between hollow sites of fcc and hcp stacking to fit 23 atomic rows in 22 lattice spacings. The fcc-hcp transition regions appear as 0.02-nm-high ridges in STM images separating the fcc from the narrower hcp region. Recently, it has been shown that a similar reconstruction of the Pt(111) surface can also be induced in the presence of a Pt gas environment down to 400 K.[25] It is observable at 300 K because the lifting of this reconstruction is kinetically hindered.[25] In analogy to these reconstructions, we thus assume that the stacking of Pt surface atoms is in a hcp pattern inside the pair of lines observed in Fig. 7(b). After a detailed analysis we conclude that at 400 K, Co nucleates and then grows preferably at the hcp regions of the reconstruction.[24]

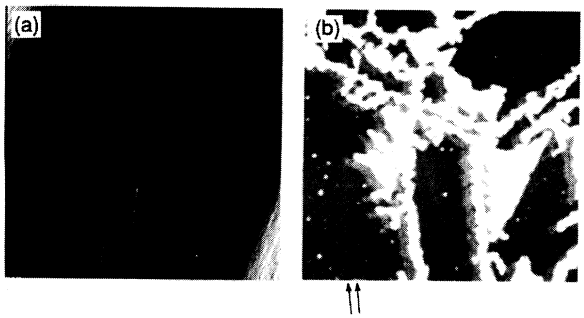

FIG. 7. (a) 0.05-ML Co deposited on Pt(111) at 400 K. Image size is 1200×1200 nm^2. (b) Detail showing Pt(111) reconstruction (marked by arrows). Image size is 100×100 nm^2.

A transition from the kinetically limited dendritic growth of Co as a function of T_s to an island growth mode probably much closer to a thermodynamic equilibrium can be observed. Figure 8(a) shows 0.4 ML grown at about $T_s=400$ K. Dendrites of similar dimensions as those shown in Fig. 7 are observable. Note that the

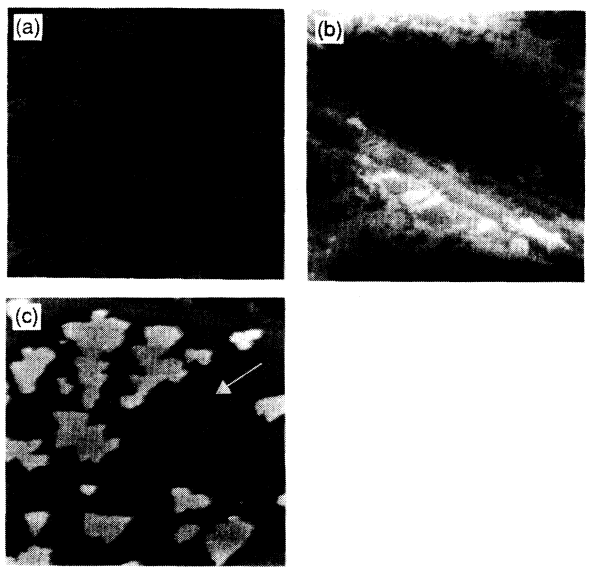

FIG. 8. 400×400-nm^2 images of Co deposited on Pt(111) at different substrate temperatures T_s: (a) $T_s=400$ K, $\Theta=0.4$ ML; (b) $T_s=500$ K, $\Theta=0.5$ ML; and (c) $T_s=600$ K, $\Theta=0.28$ ML.

threefold symmetry of dendrite arms is still dominant at this coverage, while only few sixfold-symmetric arms are observable. By depositing 0.5 ML on a substrate that is 100 K warmer, we find that this threefold symmetry is still observable [Fig. 8(b)]. The arms of the Co dendrites are, however, much wider and not as long. A detailed analysis of the images shows that the Pt reconstruction is still present, but seems to have less influence on the growth of Co than at $T_s = 400$ K. The Co islands move toward their presumed thermodynamic equilibrium shape at even higher deposition temperatures. This is demonstrated by the total lifting of the dendritic Co growth mode by depositing 0.28 ML at $T_s = 600$ K [Fig. 8(c)]: Co islands are nearly triangular and have a minimal perimeter length. These islands appear very similar in morphology to the triangular-shaped islands observed for $\Theta > 3$ ML. The Pt reconstruction, which is still observable, has little influence on the resulting morphology at this T_s. The most probable interpretation for this observation is that the mobility and binding-energy difference for Co on a fcc- or hcp-stacked Pt site is small and can be overcome by raising T_s to 600 K.

IV. SUMMARY AND CONCLUSION

From the data the following model for the nucleation and growth of Co on Pt(111) at room temperature can be deduced: Co nucleates spatially in a homogeneous manner and grows quasi-layer-by-layer up to 3 ML. Detailed analysis of the structure of first-, second-, and third-layer islands and clusters leads to the conclusion that the first-layer islands consist of locally coherent regions about 5 nm in diameter. These coherent regions are interrupted by localized defects (depressions decorated by next-layer Co clusters). This relieves some of the strain induced by the 9.7% lattice misfit. The observation of a Moiré pattern demonstrates that two-thirds of the misfit is accommodated by an isotropic contraction of the second layer of Co. The near absence of defects decorated by clusters on second- and third-layer islands additionally points to a nearly complete relief to the total lattice misfit. After the third layer, a new three-dimensional island growth mode sets in. Direct evidence proves that Co grows with a hcp stacking after the third layer. The growth of hcp Co at this coverage is a further indication of the nearly complete relaxation of the lattice misfit after 3 ML. No indication of a Co-Pt alloy formation was found up to annealing temperatures of 750 K. This is in contrast to annealing at higher temperatures, where clear indications for Co diffusion into the bulk Pt crystal were found. These annealing studies also demonstrated that room-temperature growth of Co on Pt is at least partially kinetically hindered. Evaporation at elevated substrate temperatures leads to a previously unobserved Co-induced reconstruction of the Pt(111) surface. This localized reconstruction, similar to the $22 \times \sqrt{3}$ reconstruction of Au(111), strongly influences the nucleation and growth of Co by inducing dendritic growth of threefold-symmetric Co structures with arms 3–5 nm wide and up to 250 nm long. At higher substrate temperatures (around 600 K) the kinetic limitation on the growth of Co imposed by the reconstruction is lifted, and triangular-shaped Co islands are observed.

These results clearly demonstrate the subtle effects that slight differences of the initial preparation conditions can have on the final resulting film morphology. It could be expected that besides T_s and the annealing conditions, a variation of the incident flux might also have an appreciable influence. However, we found some indications that the results presented above are valid even for an incident flux ten times larger.

Co has a substantial room-temperature mobility both on Pt and Co. This is inferred from the quasi-layer-by-layer growth mode for $\Theta < 3$ ML. Furthermore, this mobility is not reduced along step edges, resulting in the predominance of rather compact polygon-shaped islands with edges oriented along $\langle 110 \rangle$ directions independent of coverage. It has to be kept in mind, however, that the resulting shape of islands or dendrites, even though energetically favored, is not necessarily the thermodynamic equilibrium shape, but rather a result of the subtle interplay between kinetic limitations and the minimization of free energy. This is clearly shown by the evolution of the dendrite shape into a triangular island as a function of T_s (Fig. 8): the double dislocation line of the reconstruction acts as a barrier dominant at $T_s = 400$–500 K, but it is easily overcome at 600 K.

As STM lacks chemical sensitivity, we cannot exclude the local substitution of single atoms of Co by Pt. However, annealing studies indicate the absence of significant alloying or interdiffusion of Co vapor deposited on Pt(111) at 300 K, since the step height and coverage determined by STM shows no change when Co films are annealed for up to 300 min at temperatures up to 750 K. This is in contrast to annealing at higher temperatures, where drastic changes are observable both by STM and AES. The Pt-Co interface is thus sharp. This has profound consequences for theoretical models that attempt to explain the perpendicular magnetic anisotropy observed for ultrathin Co films. It would be extremely interesting to follow the next step in the growth of a multilayer structure—the deposition of Pt on a 2-ML Co film—since the deposition of 2-ML Co does not lead to a perfectly flat surface.

The correlation of magnetic properties of thin Co films with the structural findings presented above is important in itself. It holds promise of affording valuable insight into the understanding of the magnetic anisotropy of thin films. Preliminary experiments have been carried out; they indicate that the perpendicular anisotropy is strongly influenced by the morphology of the Co film. From spin-polarized scanning electron microscopy measurements we also know that the 2-ML films evaporated at 300 K are ferromagnetic with a perpendicular magnetic anisotropy.[14] This anisotropy switches to completely in-plane after 4 ML. Work in progress is aimed at correlating this with the simultaneously observed complete relaxation of stress or, alternatively, with the appearance of 3D islands at this coverage.

ACKNOWLEDGMENTS

We thank Othmar Züger and Andi Bischof for valuable assistance with instrumentation. Rolf Allenspach (who also performed the spin-SEM experiments), Jim Gimzewski, David Chambliss, and Dieter Weller contributed many useful and stimulating discussions. P.G. gratefully acknowledges a stipend by the Treubel Fonds, Basel.

[1]P. F. Carcia, A. D. Meinhaldt, and A. Suna, Appl. Phys. Lett. **47**, 178 (1985).

[2]W. B. Zeper, F. J. A. M. Greidanus, P. F. Carcia, and C. R. Fincher, J. Appl. Phys. **65**, 4971 (1989).

[3]L. Néel, J. Phys. Rad. **15**, 225 (1954).

[4]F. J. A. den Broeder, D. Kuiper, A. P. van de Mosselaer, and W. Hoving, Phys. Rev. Lett. **60**, 2769 (1988).

[5]C. Chappert and P. Bruno, J. Appl. Phys. **64**, 5763 (1988).

[6]C. H. Lee, Hui He, F. J. Lamelas, W. Vavra, C. Uher, and R. Clarke, Phys. Rev B **42**, 1066 (1990).

[7]P. F. Carcia, J. Appl. Phys. **63**, 5066 (1988).

[8]C. J. Chien, B. M. Clemens, S. B. Hagström, R. F. C. Farrow, C. H. Lee, E. E. Marinero, and C. J. Lin, in *Magnetic Thin Films, Multilayers and Surfaces,* edited by S. S. P. Parkin, MRS Symposia Proceedings No. 231 (Materials Research Society, Pittsburgh, 1992), p. 465; M. F. Toney, R. F. C. Farrow, R. F. Marks, G. Harp, and T. A. Rabedeau, in *Mechanisms of Heteroepitaxial Growth,* edited by M. F. Chisholm, R. Hull, L. J. Schowalter, and B. J. Garrison, MRS Symposia Proceedings No. 263 (Materials Research Society, Pittsburgh, 1992), p. 237.

[9]P. F. Carcia and Z. G. Li, Appl. Phys. Commun. **11**, 531 (1992).

[10]R. Q. Hwang, C. Günther, J. Schröder, S. Günther, E. Kopatzki, and R. J. Behm, J. Vac. Sci. Technol. B **10**, 256 (1992).

[11]D. D. Chambliss, K. E. Johnson, R. J. Wilson, and S. Chiang, J. Magn. Magn. Mater. **121**, 1 (1993).

[12]D. D. Chambliss, R. J. Wilson, and S. Chiang, Phys. Rev. Lett. **66**, 1721 (1991); B. Voigtländer, G. Meyer, and N. M. Amer, Phys. Rev. B **44**, 10 354 (1991); B. Voigtländer, G. Meyer, and N. M. Amer, Surf. Sci. **255**, L529 (1991); J. A. Stroscio, D. T. Pierce, R. A. Dragoset, and P. N. First, J. Vac. Sci. Technol. A **10**, 1981 (1992).

[13]J. de la Figuera, J. E. Prieto, C. Ocal, and R. Miranda, Phys. Rev. B **47**, 1304 (1993).

[14]P. Grütter, R. Allenspach, U. Dürig, and A. Bischof (unpublished).

[15]O. Züger, H. P. Ott, and U. Dürig, Rev. Sci. Instrum. **63**, 5634 (1992).

[16]J. K. Gimzewski, B. Reihl, R. R. Schlittler, and M. A. R. Tschudy, IBM Tech. Discl. Bull. **32**, 247 (1990).

[17]U. Dürig, O. Züger, and D. W. Pohl, Phys. Rev. Lett. **65**, 349 (1990); U. Dürig, O. Züger, and A. Stalder, J. Appl. Phys. **72**, 1778 (1992).

[18]P. Grütter and U. Dürig (unpublished).

[19]W. J. Kaiser and R. C. Jaklevic, Surf. Sci. **182**, L227 (1987).

[20]D. D. Chambliss, K. E. Johnson, K. Kalki, S. Chiang, and R. J. Wilson, in *Magnetic Ultrathin Films: Multilayers and Surfaces; Interfaces and Characterization,* edited by B. T. Jonker, S. A. Chambers, R. F. C. Farrow, C. Chappert, R. Clarke, W. J. M. de Jonge, T. Egami, P. Grünberg, K. M. Krishnan, E. E. Marinero, C. Rau, and S. Tsunashima, MRS Symposia Proceedings No. 313 (Materials Research Society, Pittsburgh, 1993), p. 713.

[21]T. A. Land, T. Michely, R. J. Behm, J. C. Hemminger, and G. Comsa, Surf. Sci. **264**, 261 (1992).

[22]B. A. Parkinson, F. S. Ohuchi, K. Ueno, and A. Koma, Appl. Phys. Lett. **58**, 272 (1991).

[23]C. Boeglin, A. Barbier, B. Carrière, J. P. Deville, F. Scheurer, and C. Speisser, Surf. Sci. **251/252**, 602 (1991).

[24]P. Grütter, U. Dürig, and D. D. Chambliss (unpublished).

[25]M. Bott, M. Hohage, T. Michely, and G. Comsa, Phys. Rev. Lett. **70**, 1489 (1993).

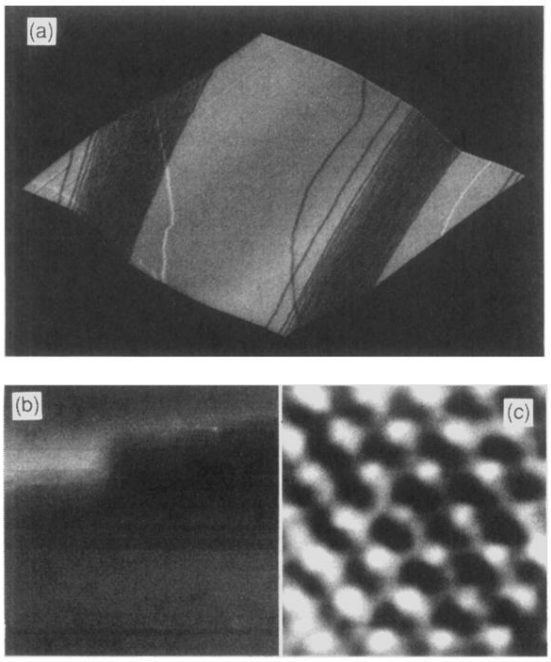

FIG. 1. (a) 1200×1200-nm^2 image of well-annealed Pt(111). Black (white) lines correspond to a single atomic steps down (up) when viewed from left to right. (b) 15×15-nm^2 image showing atomic resolution across a Pt(111) step. Horizontal stripes are due to subtle changes of the tip. (c) Low-pass filtered section of (b), showing Pt(111) atoms.

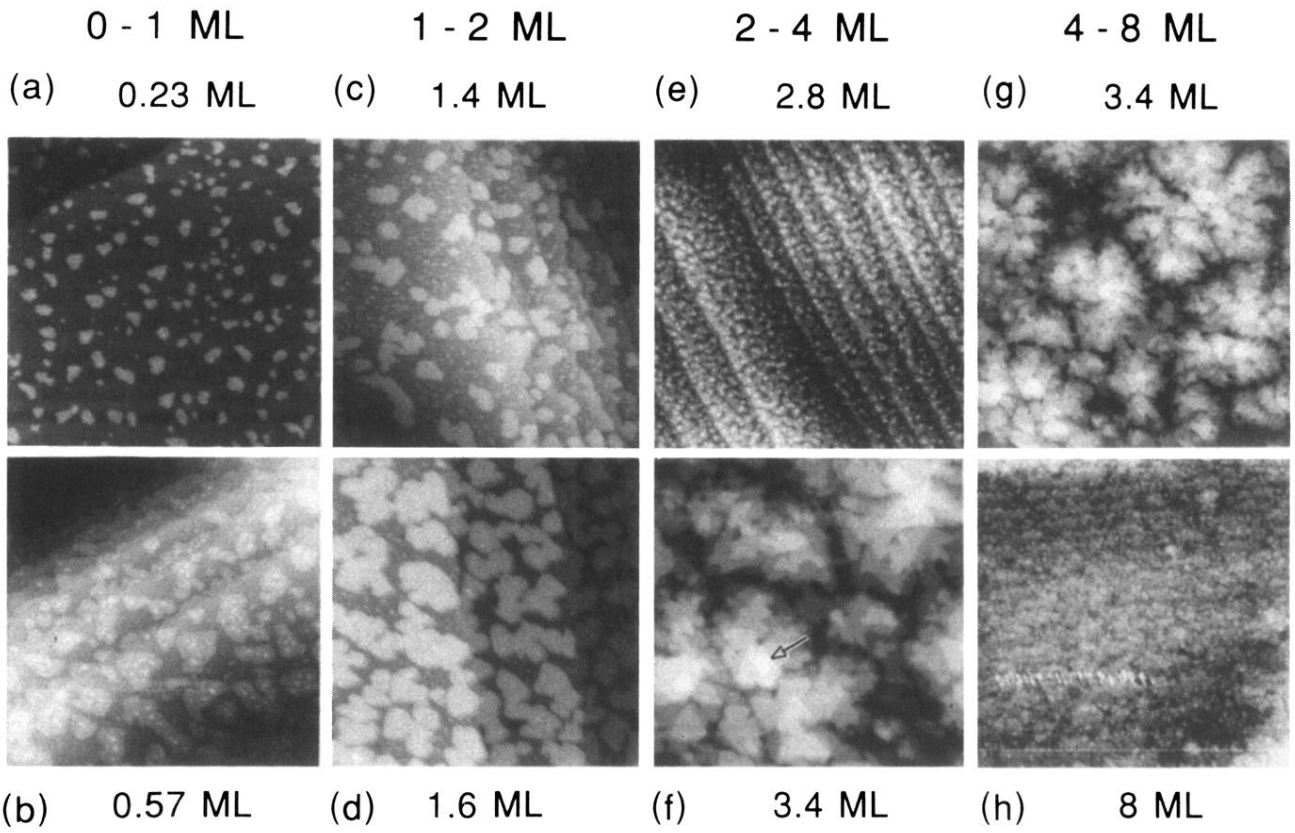

FIG. 2. Vapor deposition of Co on Pt(111) at 300 K. All images are 200×200 nm^2, except (g) and (h), which are 400×400 nm^2 in size. The arrow in (f) points to triangles stacked *UDUD* $\cdots$ (see text).

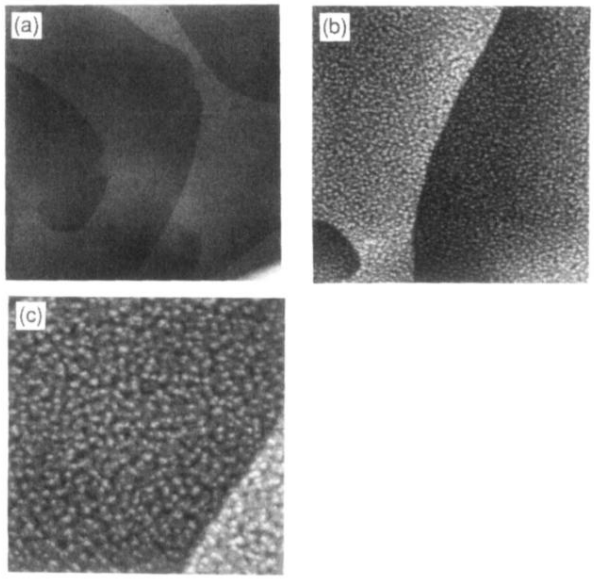

FIG. 3. Images of 2.8-ML Co on Pt(111) at a substrate region with a high density of screw dislocations. (a) 1000×1000 nm^2, (b) 400×400 nm^2, and (c) 200×200 nm^2.

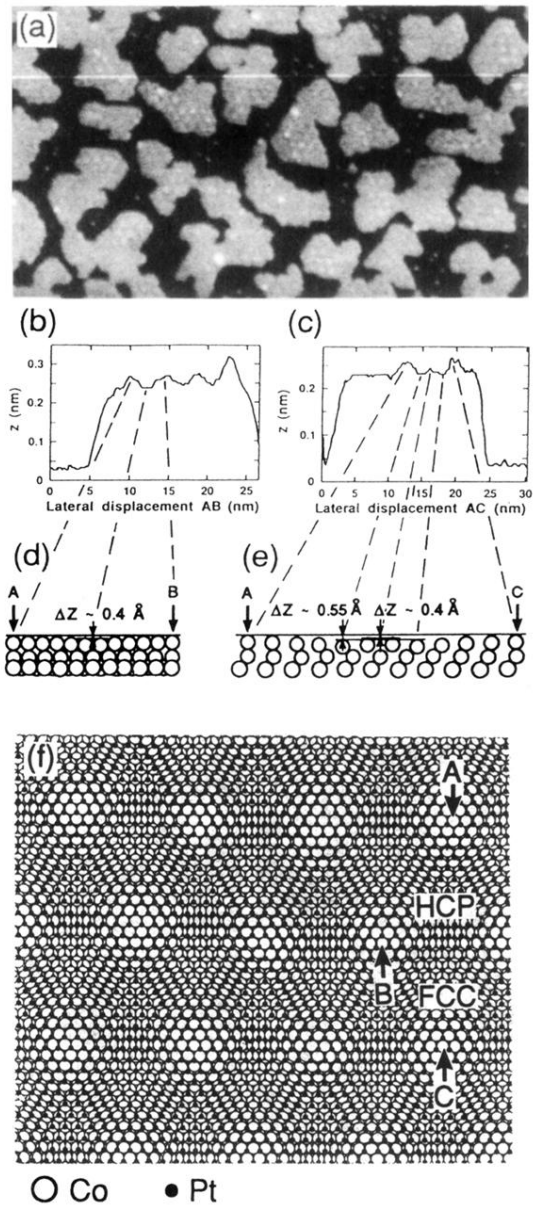

FIG. 4. $200 \times 120\text{-nm}^2$ image of 1.6 ML of Co on Pt(111) showing Moiré fringes. (a) top view; (b) experimental trace (raw data) along same direction as *AB* in 4(f); (c) experimental trace (raw data) along same direction as *AC* in (f); (d) cross section along *AB* in (f); (e) cross section along *AC* in (f); and (f) top view of the hard-sphere model of the atomic arrangement of the Pt(111) substrate, the first, and a second 10% contracted Co layer.

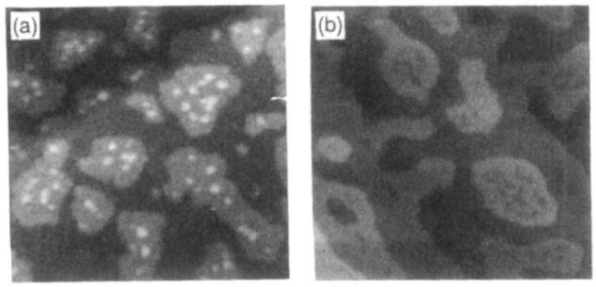

FIG. 5. Annealing study: 100×100-nm^2 image of 0.57 ML of Co on Pt(111): (a) as deposited at 300 K, and (b) after 5 min at 400 K (not at same sample position).

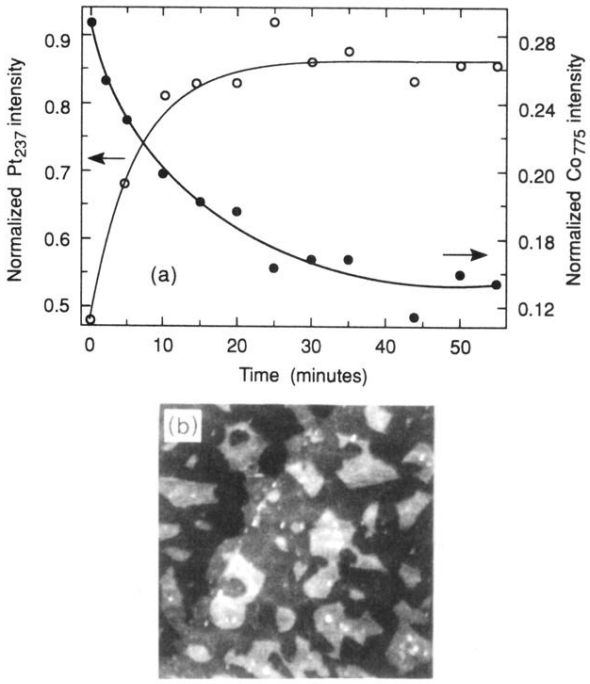

FIG. 6. (a) Evolution of 775-eV Co and 237-eV Pt Auger line intensities as a function of time at an annealing temperature of 750 K. The values are normalized to the measured pure bulk intensities. The interpolating line is a guide to the eye. (b) 400×400-nm^2 image of a 2-ML Co film after 30 min at 750 K.

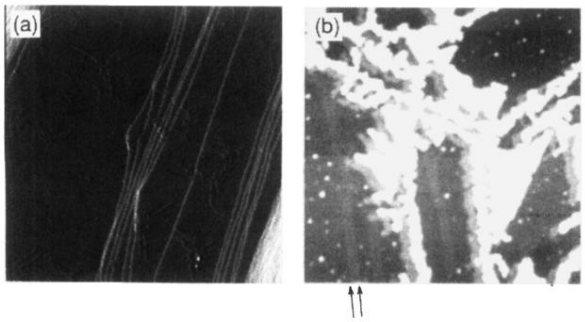

FIG. 7. (a) 0.05-ML Co deposited on Pt(111) at 400 K. Image size is 1200×1200 nm^2. (b) Detail showing Pt(111) reconstruction (marked by arrows). Image size is 100×100 nm^2.

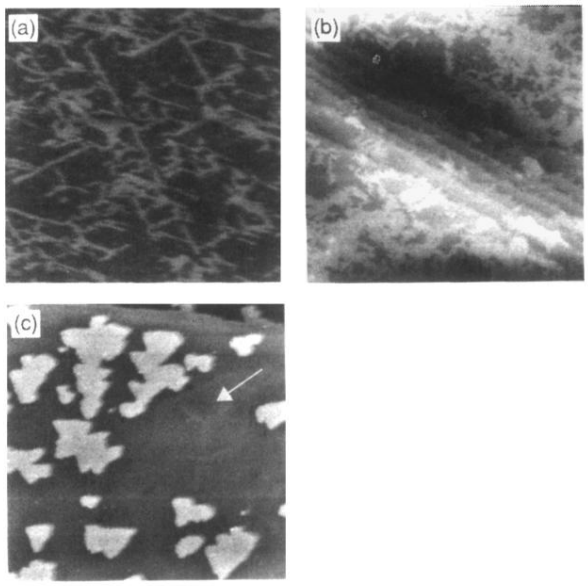

FIG. 8. 400×400-nm^2 images of Co deposited on Pt(111) at different substrate temperatures T_s: (a) $T_s=400$ K, $\Theta=0.4$ ML; (b) $T_s=500$ K, $\Theta=0.5$ ML; and (c) $T_s=600$ K, $\Theta=0.28$ ML.